GEOPHYSICS, VOL. 72, NO. 6 (NOVEMBER-DECEMBER 2007); P. C95–C104, 14 FIGS.
10.1190/1.2781619

Improving lateral and vertical resolution of seismic images by correcting for wavelet stretch in common-angle migration

Gabriel Perez[1] and Kurt J. Marfurt[2]

ABSTRACT

Long-offset or high-incident-angle seismic reflections provide us with improved velocity resolution, better leverage against multiples, less contamination by ground roll, and information that is often critical when estimating lithology and fluid product. Unfortunately, high-incident-angle seismic reflections suffer not only from nonhyperbolic moveout but also from wavelet stretch during imaging, resulting in lower-resolution images that mix the response from adjacent lithologies. For an arbitrary acoustic medium, wavelet stretch from prestack migration depends only on the cosine of the reflection angle, such that the amount of wavelet stretch will be the same for all samples of a common-reflection-angle migrated trace. Thus, we are able to implement a wavelet stretch correction by applying a simple stationary spectral shaping operation to common-angle migrated traces. We obtain such traces directly by a prestack Kirchhoff migration algorithm. Correcting for stretch effectively increases the fold of imaged data, far beyond that achieved in conventional migration, resulting in improved signal-to-noise ratio of the final stacked section. Increasing the fidelity of large incident angles results in images with improved vertical and lateral resolution and with increased angular illumination, valuable for amplitude variation with angle (AVA) and amplitude variation with offset (AVO) analysis. Finally, such large-angle images are more sensitive to and therefore provide increased leverage over errors in velocity and velocity anisotropy. These ideas were applied to prestack time migration on seismic data from the Fort Worth basin, in Texas.

INTRODUCTION

Surface seismic data are a major source of information about the subsurface. Roughly, this information has two major components: (1) seismic patterns and textures that allow us to map structure and stratigraphy and (2) seismic amplitude and frequency content that allows us to map lithology and fluid content. Quantitative reservoir characterization requires an increase in both spectral bandwidth and angular illumination. Increasing spectral bandwidth increases both the lateral and vertical resolution required for ever-smaller and/or more elusive targets. Increasing angular illumination not only increases lateral resolution, but it also contributes to improved amplitude variation with offset (AVO), anisotropy, and velocity analysis, and increases the fold of stacking and thus the leverage against both backscattered ground roll and multiples. Unfortunately, in conventional seismic acquisition and processing, there is a trade-off between increasing spectral bandwidth and angular illumination.

Conventional migration assumes that every point in the earth's subsurface is a potential scatterer, generating an idealized broadband impulse response. However, band-limited wavelets are actually the building blocks of seismic data traces. When applied to the band-limited seismic wavelet, migration based on the scatterer model spreads the data out in image space, giving rise to wavelet stretch at the farther offsets. Similar to the situation in NMO, the resulting loss of frequency content and wavelet distortion from stretch are major problems for far-offset migrated data. Typically, distortion from stretch is so large beyond offsets between about once to twice the reflection depth that imaged data are discarded by harsh muting. Although several workers present methods to alleviate NMO stretch (Dunkin and Levin, 1973; Rupert and Chun, 1975; Barnes, 1992), stretch from migration gets little attention. Trickett (2003) attacks the problem during the stacking process, thereby improving the stacked image but not delivering stretch-free prestack traces, providing increased fold of stack but none of the other desired benefits mentioned above. Swan (1997) and Dong (1999) recognize wavelet stretch as a major adverse factor in AVO.

Most efforts to mitigate the impact of wavelet stretch have focused on the improved estimation of two-term AVO intercept and gradient or three-term AVO/AVA inversion. However, Shatilo and Aminzadeh (2000), Castoro et al. (2001), Brouwer (2002), and Laz-

Manuscript received by the Editor 1 February 2007; revised manuscript received 6 June 2007; published online 3 October 2007.
[1]Formerly University of Houston, Allied Geophysics Laboratory, Houston, Texas; presently Occidental Oil and Gas, Houston, Texas. E-mail: gabriel_perez@oxy.com
[2]Formerly University of Houston, Allied Geophysics Laboratory, Houston, Texas; presently University of Oklahoma, Norman, Oklahoma. E-mail: kmarfurt@ou.edu.

aratos and Finn (2004) attempt to correct for stretch directly on the seismic data. Lazaratos and Finn (2004) and Brouwer (2002) follow approaches similar to the block-moveout method of Dunkin and Levin (1973) and correct for stretch by applying inverse spectral operators. Most of these approaches deal with offset-binned data, such that the operator is not stationary as a function of time. Hilterman and Van Schuyver (2003) and Perez and Marfurt (2005) avoid the issue of nonstationarity in prestack migration by a horizon-oriented approach similar to a local application of the block-moveout method. By an analytical derivation, Roy et al. (2005) find that migration stretch for a layered medium depends only on the cosine of the reflection angle. They make the key observation that the amount of stretch is constant for angle-binned traces, thereby allowing them to mimic Lazaratos and Finn (2004) but with a simpler and more robust stationary operator.

In this paper, using Tygel et al.'s (1994) analytical expression for migration wavelet stretch, we extend the Roy et al. (2005) approach to more arbitrary media. We start by reviewing the wavelet stretch issue as it relates to prestack migration in the context of the results of Tygel et al. (1994). We then review the correction for stretch in the common-angle domain. Next, we apply this technique to Kirchhoff prestack time migration of 3D land data acquired over the Fort Worth basin, Texas. Finally, we assess the improvement on image quality and lateral resolution using multitrace geometric seismic attributes.

UNDERSTANDING MIGRATION STRETCH

Migration stretch appears as a variation in the length of the wavelet for a given event across different (usually common-offset) bins. In the forward modeling problem, energy from two closely spaced horizontal reflectors arrives closer and closer together at progressively increasing offsets (Figure 1). The goal of many seismic imaging algorithms (such as NMO correction and prestack time migration) is to compensate for this effect by moving the close reflections at far offsets to their more widely separated positions at near offsets.

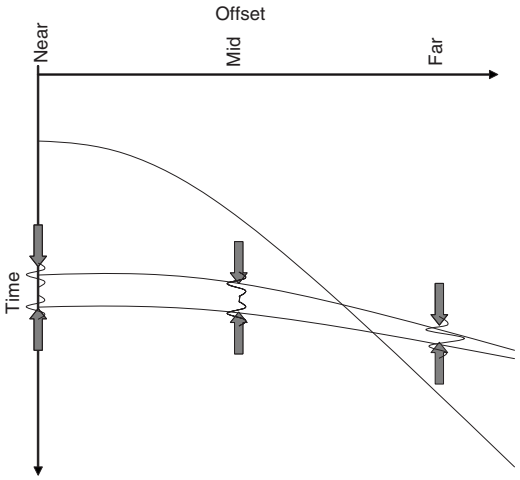

Figure 1. Causes of wavelet stretch. The traveltime between two horizontal reflectors will decrease as source-receiver offset increases. One of the objectives of seismic processing (such as NMO and prestack time migration) is to modify the time difference measured at the mid- and the far-offset traces such that it approximates that at the near-offset trace. If each of these reflectors in time is convolved with the same wavelet, these processes will generally stretch the wavelet.

A well-constructed prestack inversion algorithm attempts to place the broadband reflectivity at the correct location and to convolve it with a seismic wavelet such that it would approximately fit the measured seismic data on the surface. NMO and prestack migration algorithms are simpler — they ignore the existence of the seismic wavelet and instead assume that every time sample corresponds to an independent reflectivity. Because the algorithms work to stretch the reflectivity and because we are assuming that the wavelet is part of the reflectivity, NMO and prestack migration also stretch the wavelet.

In migration, data from many input traces contribute to the image at a given location. Differential variations in the output image location, relative to the timing of the input data samples, result in differential distortions (stretch or squeeze) of the wavelet from the input trace to the migrated trace. To illustrate this statement, Figure 2 shows prestack migration impulse responses for two input samples with a small difference in time in a constant-velocity medium. Prestack migration stretches the wavelet at large offsets, relative to that in the small-offset image. The ratio between differential variations in output image position and input data timing is much greater in the large offsets compared to the short offsets. As opposed to the small-offset case, the separation between the curves in the large-offset panel in Figure 2 decreases in the flanks relative to the separation in the center. In other words, stretch increases with dip at zero offset and decreases with dip at large offsets, as pointed out by Levin (1998) for a similar example.

In a complementary perspective, in Figure 3 we examine two vertically close positions in the image space and note that a wavelet on a large-offset data trace maps to the same piece of the image as a much broader wavelet at zero offset. The differential ratio described above

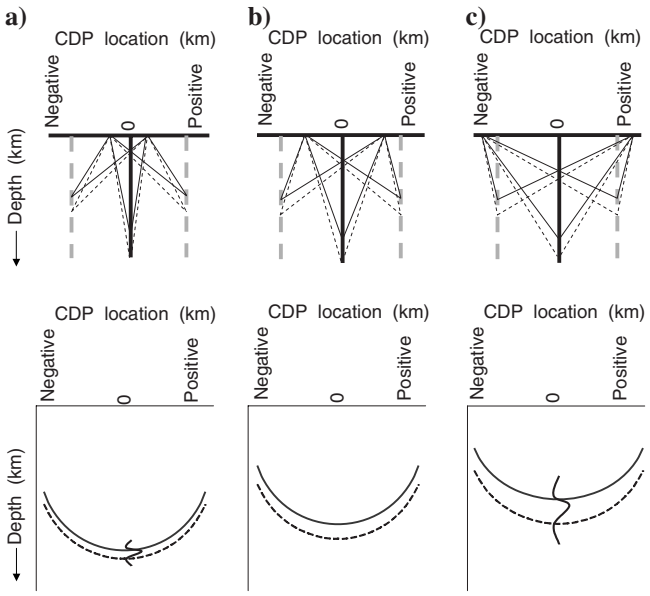

Figure 2. Migration impulse response for two close input samples and a constant-velocity medium for (a) small, (b) moderate, and (c) large common-offset gathers. Panels above each migration impulse response sketch travel paths between potential image locations (dashed gray line) and the input location in the middle (solid black line). The separation between the impulse responses is large in (c) compared to (a) so that, as sketched, a wavelet in the long-offset input data is stretched in the migrated image, relative to the short-offset wavelet.

increases with increasing offset; so once again, we observe that stretch is larger at the longer offsets, particularly if the lateral separation between the input and migrated traces is small. If the lateral separation is large, the variation in stretch across offsets is less severe. For specular reflection, lateral separation between data and image location increases with increasing dip of the imaged reflector such that the increase in stretch with offset is greatest at zero dip and less pronounced with increasing dip.

We can draw analogies with other familiar situations. First, NMO stretch is commonly stronger for longer offsets; moreover, Levin (1998) points out that moveout variation for the reflections from steeply dipping reflectors is small, so that the NMO correction introduces little stretch on the seismic wavelet. Also, poststack (i.e., approximately zero-offset) time migration causes stretch by frequency shifting in dipping reflectors, with increasing shift (i.e., larger stretch) as dip increases (Chun and Jacewitz, 1981; Barnes, 1995). Finally, regarding migration stretch, notice that the amount of wavelet stretch at a single position matters less than the relative variations in that amount between different positions. A constant value of the differential ratio discussed above would be similar to a scale change between input and output domains by a factor that is everywhere constant. In that case, if the seismic wavelet is the same for all input data traces, the output wavelet will be a scaled version of the input wavelet, but it will be the same throughout the output.

Tygel et al. (1994) describe migration stretch for prestack depth migration as a derivative that relates variations in the output image position to variations in the two-way traveltime of the input data t. Migrated seismic traces typically are displayed in the direction of the vertical axis, so they choose to compute the derivative of output image depth z (i.e., vertical image location) with respect to the two-way traveltime in the input data. Following a Kirchhoff-type approach, they find,

$$\frac{\partial z}{\partial t} = \frac{V}{2 \cos \beta \cos \theta}, \tag{1}$$

where V is the migration velocity, β is the reflection angle (i.e., the angle between the source-to-image and receiver-to-image rays), and θ is the reflector dip. Levin (1998) notes that stretch is present in prestack imaged data regardless of the migration algorithm. To be consistent with definitions for stretch in other situations as in NMO, we choose in equation 1 the inverse of the Tygel et al. (1994) measure of stretch (see also Barnes, 1995). Equation 1 quantifies the variation of migration stretch with offset and dip: The reflection angle β, and hence the factor $1/\cos \beta$, commonly increases with offset but the factor $1/\cos \theta$ increases with increasing dip. For a fixed offset, the reflection angle commonly decreases with increasing dip (see Figure 4). For steep dip, the two factors mutually balance, resulting in a relatively small variation in stretch with offset. Finally, from equation 1, differential velocity variations will result in differential stretch of the wavelet in a depth image through time-to-depth scaling by the factor $V/2$.

Levin (1998) shows that stretch dependence on the dip of the reflector is a geometric artifact associated with the conventional plotting of seismic traces along the vertical direction, similar to the familiar increase in apparent thickness of a dipping bed if measured along the vertical direction. We previously noted that Tygel et al. (1994) honor those conventions in their choice of the vertical direction as a reference to measure stretch. We can change that choice in equation 1 by projecting the derivative in the direction perpendicular to the reflector, as suggested by Levin (1998), to obtain (see Figure 5)

$$\frac{\partial r}{\partial t} = \frac{V}{2 \cos \beta}, \tag{2}$$

where r denotes the coordinate direction perpendicular to the reflector. By examining imaged data on a variable-intensity display (i.e., no traces) in a direction perpendicular to the reflector, we observe stretch dependent only on reflection angle and velocity variations. The objective of this paper is to correct for this physical component of stretch without worrying about the graphical display component. For time migration, we should not include the $V/2$ time-to-depth scaling factor, leaving only the $1/\cos \beta$ term, which is similar to the result of Roy et al. (2005) but with a more general application.

COMMON-ANGLE KIRCHHOFF MIGRATION

A significant amount of technical literature deals with computing angle-domain image gathers, with most emphasis on prestack depth

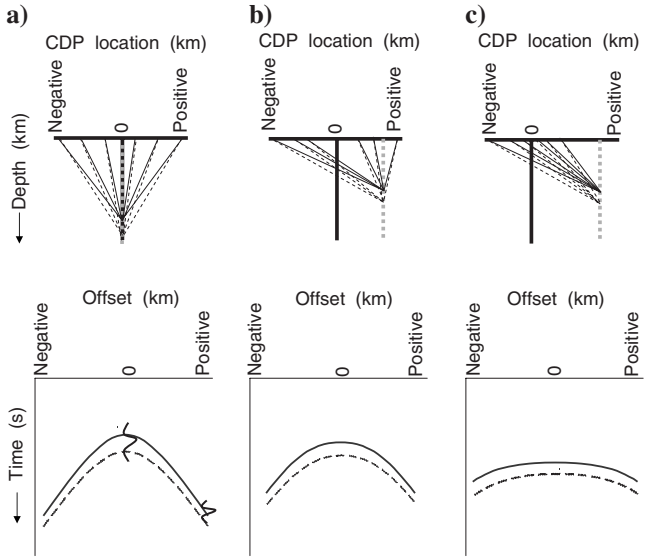

Figure 3. Raypaths and impulse response from two buried point diffractors measured on CMP-sorted gathers whose CMP location (denoted by the black solid line) is at (a) near, (b) moderate, and (c) large distance from the location of the diffractors (dashed gray line). Note how the arrival times become closer at larger offsets in (a) but are nearly parallel in (c).

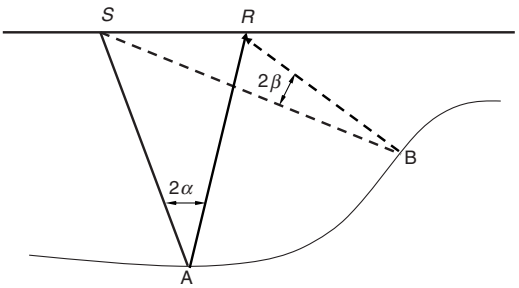

Figure 4. At a fixed offset in a medium with smooth velocity variation, the reflection angle α for the flat reflector at A is larger than the reflection angle β for the dipping reflector at B.

migration either by Kirchhoff (e.g., Brandsberg-Dahl et al., 2003) or wave-equation (e.g., Sava and Fomel, 2003) methods. Fomel and Prucha (1999) discuss some conceptual aspects of prestack time migration in the angle domain and offer an alternative implementation to that presented here.

To obtain common-angle migrated data, we modify a conventional 3D prestack-time Kirchhoff migration algorithm to output migrated traces binned by values of the angle β between the source-to-image and receiver-to-image rays (Figure 6). In contrast to common-offset migration, where a given input trace maps to a single output offset bin, each sample of a given input trace for our modified algorithm may map to a different output β bin. As common for prestack time migration, we assume the rays are straight so that the angle depends, through simple geometric expressions, on the coordinates of the source, receiver, and image points. Computation of β occurs in the innermost loop of the migration code, so this migration algorithm is more expensive computationally than one that bins over offset and/or azimuth. Appendix A provides more details on our implementation.

In common practice, a postimaging step prior to AVO analysis generates angle-binned traces after migrating the data into common-offset bins. The most common approach uses precomputed tables, also referred to as mute functions, relating angle to offset and depth or offset and time of the image. To establish this relationship in a computationally efficient way, the usual approach is to compute traveltimes in a flat-layered local approximation of the medium. This approach is accurate for specular reflections from nearly flat horizons, but it is inaccurate for strongly dipping reflectors as well as for diffractions from lateral discontinuities. In another limitation of this approach, mute functions usually are computed for a 2D model, assuming that the source, receiver, and image point are collinear and the rays between them lie in a vertical plane. In our implementation, computation of β for each input sample based on the position of source, receiver, and image points avoids this approximation.

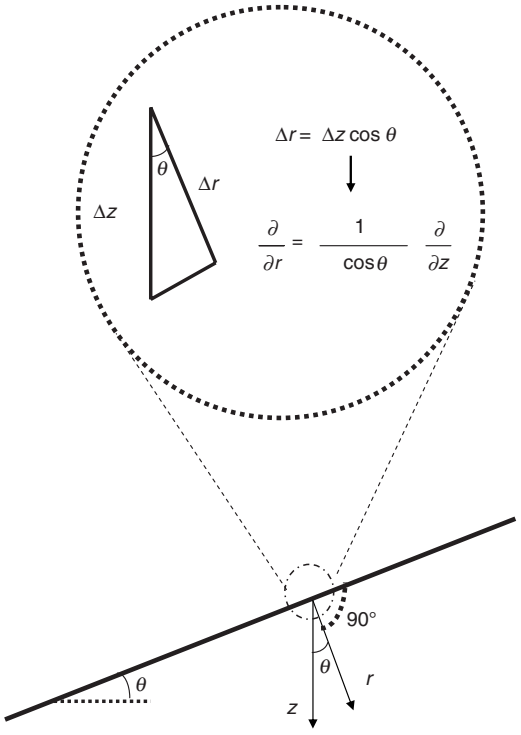

Figure 5. Projection of a vertical derivative perpendicular to the reflector.

Reconstructing the specular reflection path for every image sample allows for a more accurate postmigration transformation from offset to angle binning (J. Leveille, personal communication, 2006). An operation that is essentially the same as a prestack map demigration provides the source and receiver location for a specular ray from measurements of horizontal slowness (i.e., reflector dip) at the image sample location. In prestack time-migrated data, closed-form expressions are available for the demigration (Douma and de Hoop, 2006), after which the reflection angle can be computed from the above straight-ray geometry. Prestack depth demigration requires ray tracing, which includes angle computation. Besides the added expense of measuring reflector dips, this approach relies on the presence of an identifiable specular reflector, so that relevant events other than reflectors, such as fractures, faults, channel edges, karst, mass transport complexes, and other discontinuities, would be poorly imaged.

CORRECTION FOR STRETCH IN ANGLE-BINNED DATA

Using the result of Tygel et al. (1994), we extend the observation of Roy et al. (2005) to an arbitrary medium and observe that the amount of wavelet stretch is stationary for any common-angle binned migrated trace. This observation applies equally to prestack time and depth migration. The correction for stretch then becomes the convolution with a spectral operator such as those applied to NMO stretch by Castoro et al. (2001) and Lazaratos and Finn (2004) and to prestack imaging by Roy et al. (2005).

Following Castoro et al. (2001), we model every imaged trace as a 1D convolution of the seismic wavelet with the earth's reflectivity. For simplicity, we assume the wavelet is time invariant throughout the gather. In the frequency domain, convolution becomes multiplication, such that we can represent the imaged data as

$$D_0(f) = R_0(f)W_0(f), \tag{3}$$

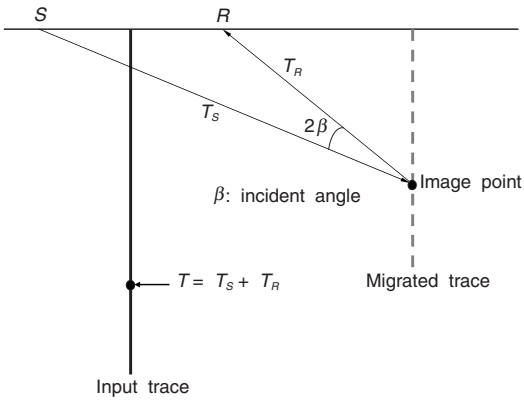

Figure 6. Kirchhoff migration involves computing the traveltimes T_S and T_R from the image point to the source and receiver positions. In prestack-time Kirchhoff migration, the rays are assumed straight, and an average velocity is used for the computation. In this case, from the source, receiver, and image-point coordinates, the incident angle can be computed as half the angle between the straight rays. Notice that the angle changes for every input trace and every image location.

$$D_\beta(f) = R_\beta(f) W_\beta(f), \tag{4}$$

where D_0 and D_β are the Fourier transforms for the reference and stretched traces and R_0 and R_β are the corresponding Fourier transforms of the reflectivity. In principle, the reference trace is the unstretched trace at normal incidence, or $\beta = 0$, and the stretched trace is that corresponding to a finite reflection angle of β. Notice that we consider angle-dependent reflectivity in equation 4. In the absence of AVO/AVA effects, $R_0(f)$ and $R_\beta(f)$ would be the same.

If we represent the unstretched wavelet as $w_0(t)$, the previous discussion shows that the stretched wavelet w_β is given by

$$w_\beta(t) = w_0(t \cos \beta). \tag{5}$$

In the frequency domain, using the Fourier scaling theorem, this becomes

$$W_\beta(f) = \frac{1}{\cos \beta} W_0\left(\frac{f}{\cos \beta}\right), \tag{6}$$

where W_0 and W_β are the Fourier transforms of the unstretched and stretched wavelet. Equations 5 and 6 are presented by Roy et al. (2005); equivalent expressions are given by Dunkin and Levin (1973), Barnes (1992), Castoro et al. (2001), and Lazaratos and Finn (2004).

The goal of the correction for stretch is to modify the wavelet in the stretched trace so that it becomes similar to the wavelet in the reference trace without modifying the reflectivity. We can formulate it as

$$\overline{D_\beta(f)} = D_\beta(f) \frac{W_0(f)}{W_\beta(f)}, \tag{7}$$

where $\overline{D_\beta(f)}$ indicates the Fourier transform of the stretch-corrected trace. The correction amounts to the application of a spectral operation, represented by equation 7, that changes the Fourier transform of the stretched wavelet into its reference counterpart. This correction makes the trace at angle β look similar to the reference trace, i.e., if there is no AVO/AVA, equation 7 provides the same result as equation 3.

For the traces in a common-reflection-point gather, the zero-angle trace should be the ideal reference since it is free of wavelet stretch. For land data, ground roll often contaminates the zero-angle incidence trace, such that we may wish to choose some other convenient angle as the reference (Roy et al., 2005). In this way, we correct for stretch in the sense that we equalize it for all traces in the gather to the amount of stretch in the reference angle. In practice, we can use a narrow stack of traces near the reference trace.

As first recognized by Roy et al. (2005), the correction for stretch in equation 7 can be implemented as a stationary operation on angle-binned migrated data. We can implement these corrections in several ways.

One way is to estimate Fourier transforms for the reference and stretched traces followed by spectral division of the reference spectrum by that of the stretched trace. This operation is the same as a division between equations 3 and 4. The result is the Fourier transform of an operator that we transform back and convolve in time with the stretched trace. Castoro et al. (2001) apply a similar procedure to offset-binned NMO-corrected traces in a nonstationary implementation. Notice that this assumes we can discard angle-dependent reflectivity variations.

Three other ways exist. One is to compute a shaping operator that matches the spectrum from the stretched trace to that of the reference trace, followed by convolution with this operator. This procedure is akin to implementing the division in equation 7 as a shaping operator; it also rests upon the assumption that we can neglect angle-dependent reflectivity variations. Another method is wavelet estimation using a model-based inversion method (e.g., Routh et al., 2003). Or we can implement equation 7 by explicitly scaling the wavelet spectrum as a function of time, computed as part of a spectral decomposition algorithm (e.g., Liu and Marfurt, 2007).

The first two procedures are straightforward to implement because they do not require sophisticated wavelet estimation. To mitigate the impact over angle-dependent reflectivity, we could select relatively short time windows in the data or select data windows where we expect that the reflectivity variations are small across angles and do not include the target horizons of interest. We have found that the spectral shaping approach based on the near-angle images improves vertical and lateral resolution of both large-angle and stacked images. It rests upon a least-squares formulation, so this shaping appears to be quite robust against noise and other limitations of the input data.

We modified the implementation of the shaping approach to compute and apply correction operators that are global and angle consistent in the sense that a single operator holds per each angle bin in the whole data set. In this way, any distortions to angle-dependent reflectivity are consistent and predictable across the whole survey, and relative trace-to-trace reflectivity variations in every common-angle subvolume are preserved.

APPLICATION TO FIELD DATA

Acquisition geometry for the survey includes a grid with 198 inlines, 219 crosslines, and a bin size of 33×33 m; average fold is about 40, and maximum offset is about 7500 m. Such high maximum offset is present only in a relatively small area in the center of the grid. For the offset range beyond 3000 m, fold is relatively low and has irregular spatial distribution. Depth to the exploration target is about 2500 m, with two-way arrival time in the 1.2–1.3 s range.

The data set available to us consisted of preprocessed (i.e., with statics and noise attenuation) common-midpoint (CMP) gathers. We processed the data twice, initially with conventional prestack time migration and then with an angle-binned implementation; the conventional migration workflow included a velocity estimation step. We used the same velocity field for conventional migration and the angle-binned migration. As appropriate for time migration, we computed velocities following a Deregowski loop approach, where we first migrated the data with a velocity field derived from the NMO-corrected velocities used in earlier time processing (Deregowski, 1990). Using this velocity field, we then restored NMO on selected gathers; an additional step of hyperbolic moveout analysis provided updated velocities, used for the final migrations.

Hyperbolic moveout is accurate enough in conventional practice, but it increasingly fails for the largest offsets, roughly beyond twice the reflector depth (Al-Chalabi, 1973), or incidence angles beyond about 45°. Departure from hyperbolic moveout in the seismic events might be even stronger in the presence of factors such as anisotropy and/or lateral velocity variation (Alkhalifah, 1997). Nonhyperbolic moveout must be addressed if one aims to image data at offset or angle ranges larger than what conventional practice commonly achieves. Conceptually, the best way to correct for nonhyperbolic

moveout is by a comprehensive imaging approach that directly addresses these factors, such as prestack anisotropic depth migration. However, that choice also demands additional work that is not very relevant to the main goal of this paper.

In our example, we had a great deal of well control and a very clear idea of the location of the target we wished to image. Therefore, we implemented a data-dependent correction for nonhyperbolic moveout. After a first migration with the velocity field defined as described above, we picked residual moveout of selected events on a sparse grid of migrated common-image gathers. At every gather location, we fit the moveout of every picked event to a polynomial in even powers of offset distance, computing coefficients for this polynomial using a least-squares procedure. We interpolated the individual coefficient values, first in time and then across gathers, to obtain coefficient values for every image location. For every input trace migrated to a given image location, we used these coefficient values and the offset distance for the input trace in the polynomial moveout expression to compute a nonhyperbolic update to the image time given by the isotropic prestack Kirchhoff migration algorithm.

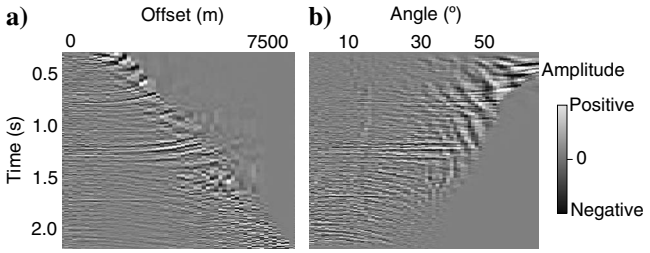

Figure 7. Common image gathers at the same location for (a) a conventional offset-binned migration and (b) the angle-binned migration that, as opposed to the common-offset migration, has also been corrected for residual moveout. Wavelet stretch is present in both.

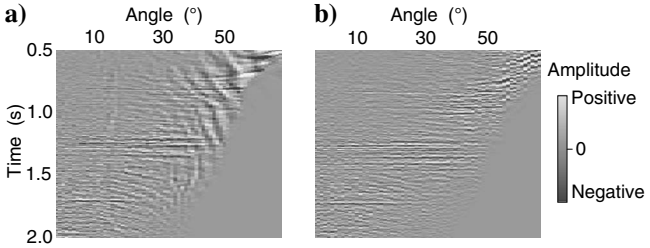

Figure 8. Common image gather (a) before and (b) after the stretch correction.

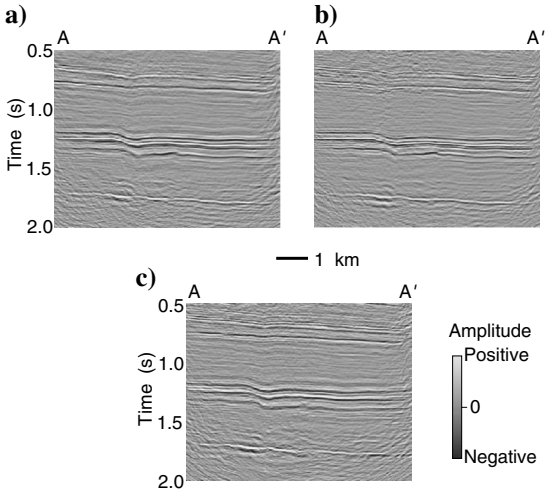

Figure 9. Comparison between stacks for a selected inline from the 3D volume for the full range of angles: (a) before and (b) after the stretch correction. (c) The full stack for the conventional offset-binned migration.

Figure 7 compares imaged gathers from a conventional offset-binned prestack migration and the residual-moveout-corrected angle-binned migration, illustrating how the correction improves imaging at the larger angles. The data-dependent residual moveout correction provides no added knowledge about the presence and magnitude of anisotropy or lateral velocity variations. However, it does generate an improved image.

For the common-angle migration, we sorted the migrated data into common-angle bins in the 0°–65° range, with 1° spacing between bins. Figures 7 and 8 show that beyond about 50°, only the shallow section above $t = 1.0$ s is imaged. As a reference for the stretch correction, we found the single trace at $\beta = 0°$ to have a poor signal-to-noise ratio. We therefore chose a stack of the traces in the 10°–15° range of angles. Instead of computing a shaping operator for every trace in the migrated data set, we computed and applied a single shaping operator for each of the 66 angles in the imaged data set (details provided in Appendix C).

To minimize the impact over AVO/AVA effects at the target horizon and for better statistics, the window for computing the shaping operator included the whole length of the traces. Figure 8 illustrates the stretch correction on the data from an angle gather. In the original migrated gather, migration stretch is readily apparent as a change in the spectral character of the data that is consistent across angles, with the far-angle traces being more stretched and appearing as lower frequency than the near-angle traces. In addition, the spectral character of the data at individual traces does not change dramatically with time, apart from the expected frequency decay likely from attenuation/transmission, which is especially common in land data. In short, the stretch in the imaged data conforms to our expectations, growing as the angle increases and being constant along time in a common-angle trace.

The shaping procedure largely corrects for migration stretch in a range of angles reaching as far as about 55°. Beyond $\beta = 55°$, illumination is poor and noise dominates. Figures 9 and 10 compare the full-range angle stacks before and after the stretch correction; the comparison includes the stack from the conventional offset-binned migration. The stack after correcting for stretch is less noisy, and the image is sharper and generally better resolved. Figure 11 shows a comparison between the partial stacks for the 35°–55° angle range, before and after the stretch correction. Notice that because of the muting applied to the imaged data binned in offset, a far-offset partial stack is not comparable to the images in Figure 11: there is no data above 1.2 s in the muted far-offset stack. The stretch correction not only helps to remove noise such as seen in the full-range stack, but it also improves the frequency content and resolution of the image. Though not shown here, improvements are not as dramatic for the smaller angle ranges. The remarkable improvement in data quality on the far-angle range is the major contribution to the improvement of the full-range stack.

In Figure 12, we examine the impact of the stretch correction in lateral resolution using coherence, a measure of the similarity between neighboring traces in a 3D data volume that provides an image of lateral changes in waveform (Chopra and Marfurt, 2006). Multi-

trace attributes such as coherence may reveal subtle geologic features that are lost in conventional images and provide a way for us to assess the lateral resolution in the migrated images generated in this work. In Figure 12, the stretch-corrected image better defines the complexity of the northeast-trending fault zones. Definition of those features is potentially very important for the exploration and development goals in the Fort Worth basin.

Using the inline coherent amplitude gradient (Chopra and Marfurt, 2006), Figures 13 and 14 further illustrate the improvement in image quality and resolution achieved with the stretch correction, as well as the variations in illumination between different angle ranges. Because of the correction, resolution improves not only for the largest 35°–55° angle range but also at intermediate angles, in the 10°–20° and 20°–35° ranges. Illumination is poorest for the smallest incidence angles, as we also see from Figures 13 and 14. Noise, particularly ground roll, dominates in this angle range. In selecting the 10°–15° angle range as a reference for the shaping in stretch correction, we avoid the noisier near-zero angles.

DISCUSSION

Variation in tuning across traces in an imaged gather also depends on the angle of incidence (Lin and Phair, 1993), so that tuning is also constant along a common-angle trace. For this reason, our stationary shaping procedure to correct for stretch also implicitly corrects for angle-dependent tuning, in the sense that the correction balances the

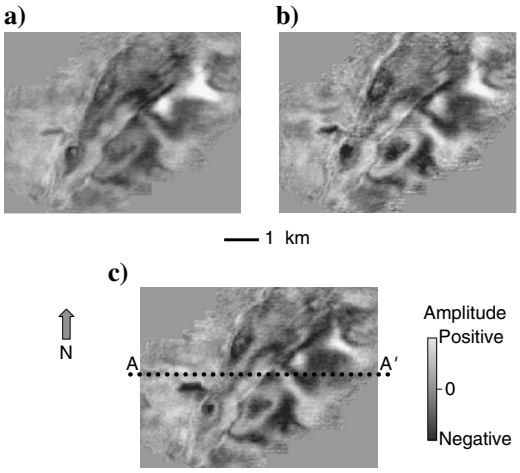

Figure 10. Comparison between time slices at 1.36 s from the stack for the full range of angles: (a) before and (b) after the stretch correction. (c) The full stack for the conventional offset-binned migration. Line AA′ shows the location of the seismic line in Figures 9 and 11.

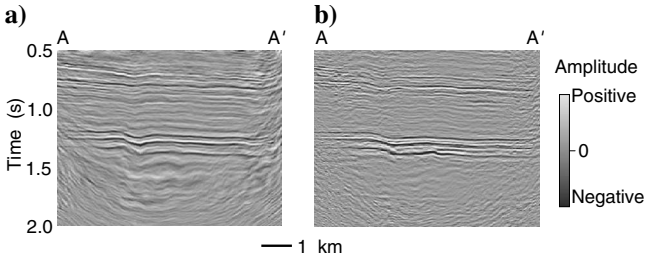

Figure 11. Comparison between the far–range (35°–55°) angle stack (a) before and (b) after the stretch correction.

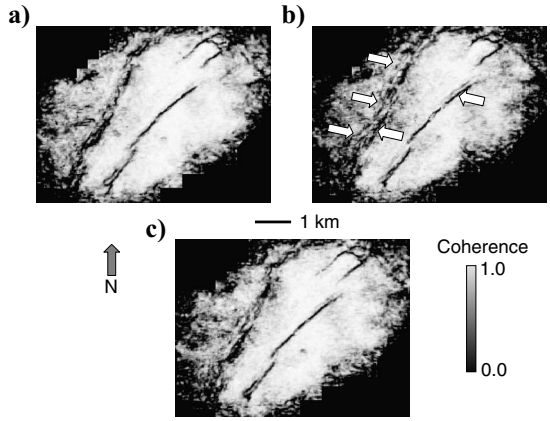

Figure 12. Comparison between coherence slices at 1.36 s for the stack on the full range of angles: (a) before and (b) after the stretch correction. (c) The coherence for the conventional offset-binned migration. Arrows in the stretch-corrected image point to locations where the image has improved.

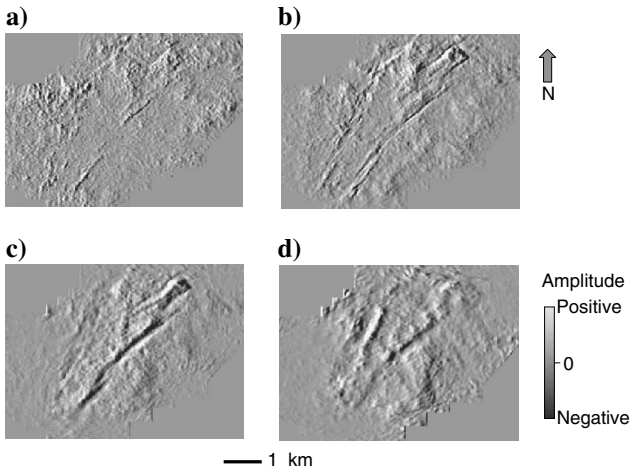

Figure 13. Time slices at 1.36 s on inline coherent amplitude gradient attribute volumes for data before the stretch correction in the (a) 0°–10°, (b) 10°–20°, (c) 20°–35°, and (d) 35°–55° angle range partial stack. Notice the increasingly smeared character of the images as angle increases as well as the relatively poorer definition on the lowest angle range.

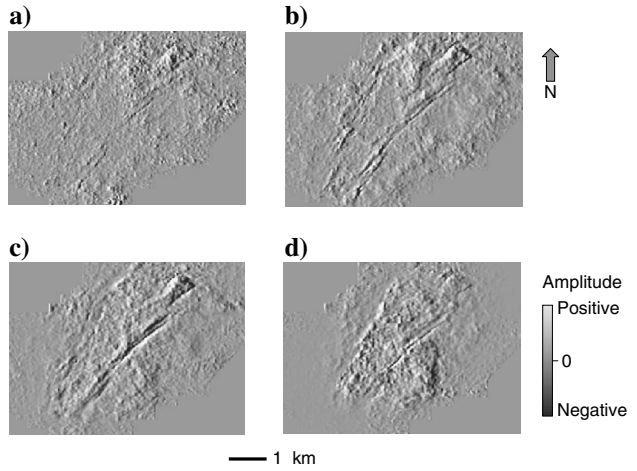

Figure 14. Images corresponding to those in Figure 13 but for data after the correction for stretch.

tuning to that at the angle used as a matching reference in computing the correction operator.

Because of the shaping character of the stretch correction operator, polarity changes or other AVO/AVA effects will not be preserved if the operator is computed and applied on a gather-by-gather basis. This is certainly a limitation of that approach and the main motivation to implement the correction through surveywide operators, one per angle bin. Such single operators equalize the distortion upon angle-dependent reflectivity, akin to the equalization in surface-consistent approaches to deconvolution and amplitude correction. In fact, the surveywide character of the computation provides greater statistical robustness than achieved in the surface-consistent formulation, whose scope is at the gather (i.e., common shot, common receiver, and/or common midpoint) scale.

If the assumption of a stable wavelet throughout every common-angle subvolume is valid, the correction equally distorts the reflectivity in every trace in the subvolume, so that relative reflectivity variations across the subvolume are preserved. In other words, AVO/AVA effects will be distorted in every individual gather, but relative variations in those effects across gathers should be preserved. In a common-image gather, the distortion on every trace will be different but smoothly varying across angles; if present, large distortions will be confined to the largest angles. Furthermore, the global correction operators are easy to preserve and use in reproducing and/or correcting for the distortion effect in later studies.

Similar to the impact over AVO/AVA present in the data, the shaping approach will also balance the spectral content of the data to that of the reference trace and, more specifically, to the frequency content of the window used for the computation, in the reference trace. As a result, the shaping will largely wipe out variations of spectral content in the data along a given angle trace and across angles arising from elastic and anelastic losses. Though one might consider it as a convenient side effect, at least for the purposes of generating an improved image, it is unlikely that such corrections correlate to, or provide insight on, the physical mechanisms causing the attenuation.

Even though the correction for stretch avoids the need to mute the data after imaging, the practice of limiting the maximum angle imaged by the migration algorithm amounts to discarding data in the largest angles during the migration itself. The basic difference is whether rejecting the data occurs during or after imaging. As in the data example we presented, choice of the maximum imaged angle in practice should include the whole range of angles imaging the target, as dictated by the acquisition geometry. Typically, those large angles not included in the migration image shallower levels of less interest. Muting data away because of stretch limits the angle illumination achieved in conventional imaging to a maximum roughly in the 30°–40° range. In this perspective, the correction for stretch pushes the upper limit of effective illumination to the maximum allowed by the acquisition.

Besides stretch, other factors can result in poor imaging and/or lack of alignment of the signal in far-offset or far-angle images before stack. These factors may include residual velocity errors and/or the need to include anisotropy in the imaging algorithm, and possibly others. Discarding the data (a common practice) reduces or eliminates the need to consider those factors. Any attempt to achieve all of the potential benefits derived from including far-offset or far-angle data must address those issues.

Although this was not the focus of our work, the combined correction for tuning and stretch improves the quality of the data for AVA/AVO and prestack inversion.

CONCLUSIONS

Prestack migration into common-reflection-angle bins results in traces that are stretched by a time-invariant (depth-invariant for depth migration) amount as a function of angle. This invariance allows correction for stretch by a stationary spectral-shaping operation. The presence of dip results in apparent stretch of the migrated data, if examined in a direction other than normal to the reflector dip. In time-migrated data, this stretch results in an apparent shift in frequency content of the data in the vertical (time) direction. We do not need to correct for this geometric and graphical presentation effect. Our correction balances the stretch across angles, thereby increasing the frequency content and S/N of far-angle imaged data. Muting these data is no longer necessary, so the correction increases the range of angle illumination and provides added effective fold that improves the quality and lateral and vertical resolution of the stacked image. The correction also balances angle-dependent tuning across angles. Computing the correction operators in a global, angle-dependent fashion minimizes the impact upon angle-dependent reflectivity.

Fully achieving the potential of this technique requires that the migration properly accounts for nonhyperbolic moveout. Extending the range of angles (implicitly offsets) beyond that achieved in conventional imaging presents additional challenges to address — in particular, estimating anisotropy and polarization changes. Such estimates and corrections require more work, but they also provide additional information about the subsurface.

ACKNOWLEDGMENTS

The authors thank the sponsors of AGL and the Petroleum Research Fund for their support and Devon Energy for permission to use their data.

APPENDIX A

PSTM IMPLEMENTATION AND OPENING ANGLE COMPUTATION

The migration image is computed as

$$m_i(t_i) = \sum_{sg} a(t, r_{sg}) \frac{\partial}{\partial t} d_{sg}(t - t_{si} - t_{ig}), \qquad \text{(A-1)}$$

where m_i is the migrated image and t_i the migrated time at image point i, $(\partial/\partial t)d_{sg}(t - t_{si} - t_{ig})$ is the value at time $t_{si} + t_{ig}$ of the time-differentiated data trace collected at receiver g from source s, t_{si} is the one-way traveltime from the source to the image point, t_{ig} is a similar time from the image point to the receiver, r_{sg} is the source-receiver offset, and a is a composite amplitude factor that includes the obliquity factor, antialias filtering and rejection of refracted energy. In the migration corrected for residual moveout, $m_i(t_i)$ is changed to $m_i(t_i - rmo(t_i, r_{sg}))$ where $rmo(t_i, r_{sg})$ is a residual moveout correction dependent on image time and source-receiver offset (see Appendix B).

One-way traveltimes are computed assuming a straight raypath from the source or receiver to the image point and a simple scaling to image-point depth from image time using the local migration velocity:

$$t_{si} = \sqrt{\frac{r_{si}^2}{V^2} + \left(\frac{t_i}{2}\right)^2} \quad \text{and} \quad t_{ig} = \sqrt{\frac{r_{ig}^2}{V^2} + \left(\frac{t_i}{2}\right)^2} \tag{A-2}$$

where V is the migration velocity. The values

$$r_{si} = \sqrt{(x_i - x_s)^2 + (y_i - y_s)^2} \quad \text{and}$$
$$r_{ig} = \sqrt{(x_g - x_i)^2 + (y_g - y_i)^2} \tag{A-3}$$

are the lengths of the surface projections of the source-to-image and receiver-to-image straight rays. The algorithm assumes that source and receiver are placed at the surface with coordinates $(x_s,y_s,0)$ and $(x_g,y_g,0)$, respectively. The image-point coordinates are (x_i,y_i,z_i); by the simple time-depth conversion mentioned above, $z_i = Vt_i/2$.

For angle binning, we compute the opening angle also from the straight-ray assumption by the dot product formula:

$$2\beta = \cos^{-1}\left(\frac{\mathbf{t}_{si} \cdot \mathbf{t}_{ig}}{t_{si} t_{ig}}\right), \tag{A-4}$$

where $\mathbf{t}_{si}$ and $\mathbf{t}_{ig}$ are vectors corresponding to the straight rays from the source to the image point and from the image point to the receiver. For convenience, the computation takes the vectors scaled to one-way traveltime. The magnitudes of these scaled vectors are the one-way traveltimes t_{si} and t_{ig}, and their components are

$$\mathbf{t}_{si} = \left(\frac{x_i - x_s}{\frac{V}{2}}, \frac{y_i - y_s}{\frac{V}{2}}, t_i\right) \quad \text{and}$$
$$\mathbf{t}_{ig} = \left(\frac{x_g - x_i}{\frac{V}{2}}, \frac{y_g - y_i}{\frac{V}{2}}, t_i\right). \tag{A-5}$$

APPENDIX B

POLYNOMIAL FIT TO RESIDUAL MOVEOUT PICKS

Timing of events picked in prestack time migration (PSTM) common-image gathers is assumed to conform to the following polynomial model:

$$T^2(x) = t_0^2 + a_2x^2 + a_4x^4 + a_6x^6 + a_8x^8 = \sum a_k x^k$$
$$k = 0,2,4,6,8, \tag{B-1}$$

where $T(x)$ is the time of the event at a position x and a_k are coefficients to be determined. Notice that $a_0 = t_0^2$, where t_0 is the timing for the event at $x = 0$.

The available data is a set $\{t_j\}$ of picks for the event at a series of discrete positions $\{x_j\}$:

$$\{t_j\} = \{t_j(x_j)\} = \{t_1(x_1),t_2(x_2), \ldots ,t_N(x_N)\} \quad j = 1, \ldots ,N,$$

where N is the total number of picks on each event. Values for the coefficients a_k for each event are determined by a least-squares fit of the picks to the model in equation B-1:

$$\text{minimize } F = \sum [t_j^2 - T^2(x_j)]^2 \text{ with respect to } a_k$$
$$k = 0,2,4,6,8. \tag{B-2}$$

A necessary condition for equation B-2 is that partial derivatives with respect to a_k become zero:

$$\frac{\partial F}{\partial a_k} = 0 \quad k = 0,2,4,6,8. \tag{B-3}$$

This condition becomes

$$\sum \{x_j^k [t_j^2 - T^2(xj)]\} = 0 \quad k = 0,2,4,6,8. \tag{B-4}$$

For each value of k, expanding this last expression using equation B-1 and collecting factors for each a_k, we arrive at a system of linear equations that in matrix form can be written as

$$\begin{bmatrix} N & \sum x_j^2 & \sum x_j^4 & \sum x_j^6 & \sum x_j^8 \\ \sum x_j^2 & \sum x_j^4 & \sum x_j^6 & \sum x_j^8 & \sum x_j^{10} \\ \sum x_j^4 & \sum x_j^6 & \sum x_j^8 & \sum x_j^{10} & \sum x_j^{12} \\ \sum x_j^6 & \sum x_j^8 & \sum x_j^{10} & \sum x_j^{12} & \sum x_j^{14} \\ \sum x_j^8 & \sum x_j^{10} & \sum x_j^{12} & \sum x_j^{14} & \sum x_j^{16} \end{bmatrix} \begin{bmatrix} t_0^2 \\ a_2 \\ a_4 \\ a_6 \\ a_8 \end{bmatrix}$$
$$= \begin{bmatrix} \sum t_j^2 \\ \sum t_j^2 x_j^2 \\ \sum t_j^2 x_j^4 \\ \sum t_j^2 x_j^6 \\ \sum t_j^2 x_j^8 \end{bmatrix}. \tag{B-5}$$

Solving the system of equations provides values of the polynomial coefficients a_k for each event. In our implementation, we used routines from Press et al. (1987) to solve equation B-5 by standard LU decomposition techniques.

The polynomial coefficients thus found depend on the location of the image gather i and the image time of the event t_0. Interpolation and smoothing over space and time provides 3D cubes of coefficient values. At every image location, a residual moveout correction that depends on image time and offset can be computed as

$$\text{RMO}(t_0,x) = T(x) - t_0, \tag{B-6}$$

where $T(x)$ is computed using equation B-1 and the a_k values are from the coefficient cubes.

APPENDIX C

MULTITRACE SHAPING FILTER

Given an input signal $w(t)$ and a desired output signal $d(t)$, convolution of $w(t)$ with a shaping filter $f(t)$ gives an estimate of $d(t)$ that is optimum in some sense. Formulation of convolution as a matrix operation leads to the following representation (Claerbout, 1976):

$$\mathbf{W}\mathbf{f} \approx \mathbf{d}, \tag{C-1}$$

where $\mathbf{f}$ and $\mathbf{d}$ are column vectors with the samples of $f(t)$ and $d(t)$ and where $\mathbf{W}$ is a matrix whose columns are shifted-down versions of the samples of $w(t)$. Use of the $\approx$ symbol means that expression C-1 does not represent an identity but a best-fit approximation. Formulation as a least-squares optimization results in an instance of the well-known normal equations:

$$(\mathbf{W^T W})\mathbf{f} = \mathbf{W^T d}, \tag{C-2}$$

where $\mathbf{W^T}$ is the transpose of $\mathbf{W}$. The product $\mathbf{W^T W}$ is a Toeplitz matrix whose diagonals contain the samples of the autocorrelation of $w(t)$, and $\mathbf{W^T d}$ is a column vector with the samples of the crosscorrelation of $w(t)$ and $d(t)$. Levinson recursion (Claerbout, 1976) provides an efficient solution of equation C-2 for the short filters used in spectral shaping.

For ease of exposition, we illustrate the computation of a single shaping filter for many traces for the simple case of two traces: We want to compute a single filter $g(t)$ to match the two input signals $w_1(t)$ and $w_2(t)$, respectively, to the two desired outputs $d_1(t)$ and $d_2(t)$. The matrix representation of the problem is

$$\begin{bmatrix} \mathbf{W}_1 \\ \mathbf{W}_2 \end{bmatrix} \mathbf{g} = \begin{bmatrix} \mathbf{d}_1 \\ \mathbf{d}_2 \end{bmatrix} \tag{C-3}$$

where $[\mathbf{W}_1 \mathbf{W}_2]$ and $[\mathbf{d}_1 \mathbf{d}_2]$ are built from $\mathbf{W}_1$ and $\mathbf{W}_2$ and from $\mathbf{d}_1$ and $\mathbf{d}_2$, respectively, by putting one on top of the other, i.e., each column of $[\mathbf{W}_1 \mathbf{W}_2]$ is a vector with the elements in the corresponding column of $\mathbf{W}_1$ followed by the elements in that column in $\mathbf{W}_2$. Similarly, $[\mathbf{d}_1 \mathbf{d}_2]$ is a column vector with the samples of $\mathbf{d}_1$ followed by the samples in $\mathbf{d}_2$.

It is straightforward but tedious to show by direct multiplication that the normal equations for this problem also result in a Toeplitz matrix equation where the left-hand side matrix contains in the diagonals the sum of the samples of the autocorrelations $w_1(t)^* w_1(t)$ and $w_2(t)^* w_2(t)$. In the same way, the right-hand side vector contains the sum of the samples in the crosscorrelations $w_1(t)^* d_1(t)$ and $w_2(t)^* d_2(t)$. Extension to any number of traces is immediate. The computation of a global operator for every common-angle subvolume amounts to solving a problem equivalent to a standard shaping filter estimation in which the autocorrelation term consists of the sum of the autocorrelations for all traces in the volume and, similarly, the crosscorrelation term becomes the sum of all the crosscorrelations between data and reference traces.

REFERENCES

Al-Chalabi, M., 1973, Series approximation in velocity and traveltime computations: Geophysical Prospecting, **21**, 783–795.

Alkhalifah, T., 1997, Velocity analysis using nonhyperbolic moveout in transversely isotropic media: Geophysics, **62**, 1839–1854.

Barnes, A. E., 1992, Another look at NMO stretch: Geophysics, **57**, 749–751.

——, 1995, Discussion on "Pulse distortion in depth migration," by M. Tygel, J. Schleicher, and P. Hubral (GEO-59-10-1561-1569): Geophysics, **60**, 1942–1947.

Brandsberg-Dahl, S., B. Ursin, and M. V. de Hoop, 2003, Seismic velocity analyis in the scattering angle/azimuth domain: Geophysical Prospecting, **51**, 295–314.

Brouwer, J. H., 2002, Improved NMO correction with a specific application to shallow-seismic data: Geophysical Prospecting, **50**, 225–237.

Castoro, A., R. E. White, and R. Thomas, 2001, Thin-bed AVO: Compensating for the effects of NMO on reflectivity sequences: Geophysics, **66**, 1714–1720.

Chopra, S., and K. J. Marfurt, 2006, Seismic attributes for prospect identification and reservoir characterization: SEG.

Chun, J. H., and C. A. Jacewitz, 1981, Fundamentals of frequency-domain migration: Geophysics, **46**, 717–733.

Claerbout, J., 1976, Fundamentals of geophysical data processing: Blackwell Scientific Publications, Inc.

Deregowski, S. M., 1990, Common-offset migrations and velocity analysis: First Break, **8**, 224–234.

Dong, W., 1999, AVO detectability against tuning and stretching artifacts: Geophysics, **64**, 494–503.

Douma, H., and M. V. de Hoop, 2006, Explicit expressions for prestack map time migration in isotropic and VTI media and the applicability of map depth migration in heterogeneous anisotropic media: Geophysics, **71**, no. 1, S13–S28.

Dunkin, J. W., and F. K. Levin, 1973, Effect of normal moveout on a seismic pulse: Geophysics, **28**, 635–642.

Fomel, S., and M. Prucha, 1999, Angle-gather time migration: Stanford Exploration Project report SEP 100, 141–151.

Hilterman, F., and C. Van Schuyver, 2003, Seismic wide-angle processing to avoid NMO stretch: 73rd Annual International Meeting, SEG, Expanded Abstracts, 215–218.

Lazaratos, S., and C. Finn, 2004, Deterministic spectral balancing for high-fidelity AVO: 74th Annual International Meeting, SEG, Expanded Abstracts, 219–223.

Levin, S. A., 1998, Resolution in seismic imaging: Is it all a matter of perspective?: Geophysics, **63**, 743–749.

Lin, T. L., and R. Phair, 1993, AVO tuning: 63rd Annual International Meeting: SEG, Expanded Abstracts, 727–730.

Liu, J., and K. J. Marfurt, 2007, Instantaneous spectral attributes to detect channels: Geophysics, **72**, no. 2, P23–P31.

Perez, G., and K. J. Marfurt, 2005, Improving vertical and lateral resolution by stretch-free, horizon-oriented imaging: 75th Annual International Meeting, SEG, Expanded Abstracts, 1834–1837.

Press, W. H., B. P. Flannery, S. A. Teukolsky, and W. T. Vetterling, 1987, Numerical recipes: The art of scientific computing: Cambridge University Press.

Routh, P., P. Anno, R. Baumel, and J. Chavarria, 2003, Inversion for source wavelet and AVA parameters from prestack seismic data: 73rd Annual International Meeting, SEG, Expanded Abstracts, 698–701.

Roy, B., P. Anno, R. Baumel, and J. Durrani, 2005, Analytic correction for wavelet stretch due to imaging: 75th Annual International Meeting, SEG, Expanded Abstracts, 234–237.

Rupert, G. B., and J. H. Chun, 1975, The block move sum normal moveout correction: Geophysics, **40**, 17–24.

Sava, P. C., and S. Fomel, 2003, Angle-domain common-image gathers by wavefield continuation methods: Geophysics, **68**, 1065–1074.

Shatilo, A., and F. Aminzadeh, 2000, Constant normal-moveout (CNMO) correction: A technique and test results: Geophysical Prospecting, **48**, 473–488.

Swan, H. W., 1997, Removal of offset-dependent tuning in AVO analysis: 67th Annual International Meeting, SEG, Expanded Abstracts, 175–178.

Trickett, S., 2003, Stretch-free stacking: 73rd Annual International Meeting, SEG, Expanded Abstracts, 2008–2011.

Tygel, M., J. Schleicher, and P. Hubral, 1994, Pulse distortion in depth migration: Geophysics, **59**, 1561–1569.